Aerodynamic Modelling of Unmanned Aerial System through Nonlinear Vortex Lattice Method, Computational Fluid Dynamics and Experimental Validation - Application to the UAS-S45 Bàlaam: Part 2.

Maxime Alex Junior KUITCHE[1], Ruxandra Mihaela BOTEZ*,[1], Arthur GUILLEMIN[1], David COMMUNIER[1]

*Corresponding author
[1]ETS, Laboratory of Active Controls, Avionics and AeroServoElasticity LARCASE, 1100 Notre Dame West, Montreal, Que., Canada, H3C-1K3, maxime-alex-junior.kuitche.1@ens.etsmtl.ca, ruxandra.botez@etsmtl.ca*, arthur.guillemin.ag@gmail.com, david.communier.1@ens.etsmtl.ca

DOI: 10.13111/2066-8201.2020.12.2.9

Received: 23 January 2020/ Accepted: 06 March 2020/ Published: June 2020

Abstract: *This paper presents a comparison of a new non-linear formulation of the classical Vortex Lattice Method and a Computation Fluid Dynamics analysis in predicting the aerodynamic behaviour of an Unmanned Aerial System. The Computation Fluid Dynamics analysis used structured grid, for the airfoil, study and unstructured grid obtained from a grid convergence study, for the entire Unmanned Aerial System, that are needed to predict the aerodynamic coefficients. The Spalart-Allmaras and the k-ω models were used as turbulence models. The results have shown a close agreement between the methods presents and have indicated that the new formulation is adequate for aerodynamic model estimation.*

Key Words: *Aerodynamic modelling, Computational Fluid Dynamics analysis, ANSYS FLUENT, UAS-S45*

1. INTRODUCTION

Computational Fluid Dynamics (CFD) analysis began to be considered in the last 50 years of the 20th century with the advancement of computing capabilities.

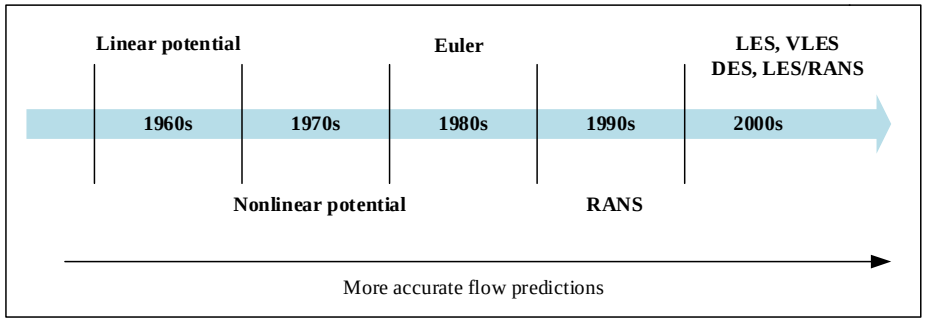

Fig. 1 Historical development of CFD

Since the 1970s, the development of numerical algorithms has allowed a rapid progression of the CFD studies. From the Lax-Wendroff and MacCormack method for solving compressible Navier-stokes equations to the Spalart detached-eddy simulation (DES) [1], the CFD studies have evolved in many ways, including structured and unstructured meshing, implicit time-integration schemes, approximate factorization, total variation diminishing-like scheme, flux vector splitting, and flux difference splitting. Figure 1 shows the evolution of the CFD methods from the linear potential method, in the 1960s, to the Large Eddy-Simulation (LES), Very Large Eddy-Simulation (VLES), Detached-Eddy Simulation (DES) and Reynold Average Navier-Stokes (RANS) methods in the 2000s. The success of the CFD in solving Navier-Stokes equations and in accurately predicting the dynamic flow around an aircraft has attracted the interest of many researchers. The CRIAQ MDO 505 [2–4] project was realized in our Research Laboratory in Active Controls, Avionics and Aeroservoelasticity (LARCASE) of the ETS in collaboration with the Ecole Polytechnique de Montréal, the University of Naples, Bombardier Aerospace, Thales Canada, Alenia Aeronautica, the IAR-NRC and the Italian Institute for Research in Aerospace CIRA. It dealt with the application of the morphing wing technique on a real wing of a Bombardier aircraft. The objective of this project was to demonstrate the aerodynamic and structural efficiency of a wing with a morphing upper surface. The wing characteristics were the following: span = 1.5m, root chord = 1.5m, sweep angle = 8deg. The upper surface of the wing was modified between 20% and 60% of the chord by means of a flexible skin deformed by a mechanical system. The flexible skin [5, 6] was composed of carbon fibre composite materials. The deformation system consisted of longitudinal members and ribs made from an aluminium alloy [2]. The numerical simulations were performed using a CFD analysis with a turbulence model able to predict the laminar-to-turbulent flow transition over the wing. This model included a fine mesh grid generation on the morphing surface that also had a grid convergence study. The Reynolds Averaged Navier-Stokes (RANS) equations with a k-ω SST model were applied for the flow analysis. Very good agreement was obtained between the numerical and the experimental results, with an average prediction error of the flow transition of approximately 5% of the chord. Both numerical and experimental results have shown that the morphing technique delayed the transition point location from 3% to 9% of the chord, which represented a considerable reduction in the total drag. Boelens [7] performed a CFD analysis while Anton et al. [8] performed a fluid dynamics analysis on the X-31 aircraft at high angle of attack. The aim of the analysis was to determine whether or not the leading-edge details and the flap gaps needed to be taken into account for the X-31 wind tunnel model in order to properly simulate the flow around its configuration. A numerical investigation was made for three different geometries of the X-31 wind tunnel configuration with: 1) all leading-edge flap gaps, 2) only the longitudinal leading edge flap gaps, and 3) no leading edge flap gaps. The NLR's Cartesian mapping grid technique [9] was used to generate a structured mesh for each geometry. This technique represents the geometry using "Cartesian blocks". The first layer of blocks around the geometry, and the field blocks in the physical space are automatically generated. The quality of the grid can then be improved by using an elliptic smoothing algorithm. The solver ENSOLV [10] was used for flow simulation. The turbulent model was a Turbulent Non-Turbulent (TNT) k-ω model [11]. The numerical analysis results were compared to the experimental results for specific flight conditions: Mach number = 0.18, Reynolds number based on the mean aerodynamic chord Re = 2.07 million and a range of angles of attack from -5° to 55°. These results indicated that for an angle of attack less than 12°, for all the configurations, the leading edge did not have an effect. The effect of the leading-edge flap configuration was observed for angles of attack larger than 12°, where some vortices dues to the longitudinal flap gaps were created.

Numerical analysis and experimental tests confirmed the very good agreement of these results. Panagiotou et al. [12] realized a winglet design and optimization methodology for a Medium Altitude Long Endurance (MALE) UAV. This methodology was also applied on to the Hellenic Civil Unmanned Aerial Vehicle (HCUAV). Initially, the wing contribution to the total drag was 40% at a trim condition and between 30% and 70% for angle of attack. The aim of their work was to reduce the drag contribution in order to maximize the flight time and the flight operation range. Six different wing configurations with the winglet were investigated by changing the cant, the toe and the sweep angle of the winglet. For each configuration, a mesh grid of 3,000,000 nodes was generated in order to model the phenomena inside the boundary layer. The aerodynamic calculations were performed using the flow solver ANSYS CFX with the Spalart-Allmaras turbulence model. The study was conducted for the loiter phase condition: range of angles of attack from -8° to 16°, speed, V=140km/h and flight altitude alt = 20,000 m, which corresponds to a Reynolds number of 1.8×10e6 based on the mean aerodynamic chord. A significant increase of the L/D (lift to drag) ratio was achieved. This performance improvement corresponded to an increase of 10% in the total flight time.

The methodology was applied to an unmanned aerial system, the UAS-S45, designed and manufactured by Hydra Technologies [13, 14]. The UAS-S45 provides surveillance and security capabilities for military and civilian purposes. General information regarding the UAS-S45 is presented in Table 1, while the UAS- S45 is shown in Figure 2.

Fig. 2 Hydra Technologies UAS-S45 Bàlaam

Table 1. General Characteristics of the UAS-S45

Specification	**Value**
Wing span	6.11 m
Wing area	2.72 m²
Total length	3.01 m
Mean aerodynamic chord	0.57 m
Empty weight	57 kg
Maximum take-off Weight	79.6 kg
Loitering airspeed	55 knots
Service ceiling	20, 000 ft
Operational range	120 km

The CFD analysis is explained in Sections 2 and 3. The results are presented in Section 4 and are followed by the Conclusion.

2. CFD ANALYSIS. GRID GENERATION

The accuracies of a structured and an unstructured mesh were investigated by Rakowitz and Eisfeld [15]. They studied the aerodynamic forces and moments of the DLR-F4 wing-body configuration. The DLR-F4 was meshed with unstructured TAU code [16] and structured

FLOWer [17] code. Three different solver models were used: the Wilcox-kw, the kw-linearized stress and the Spalart-Allmaras models. The numerical data obtained by the use of these models was compared to experimental data collected in first AIAA Drag Prediction Workshop (DPW) in Anaheim, California [18]. The results have shown that for a test case of Mach number M = 0.75 and lift coefficient C_L = 0.5, where the influence of the transition was neglected, the unstructured and the structured codes gave almost identical predictions with the three different turbulence models. For a test case of Mach number M = 0.75 at a range of angle of attack from -3 deg to 2 deg with an increment 1 deg, and for which the transition and the turbulence effects were taken into account, the lift coefficient obtained with the structured grid has matched the experimental data, whereas the unstructured grid overestimated the lift coefficient by approximately 15%. Therefore, when meshing an aircraft for computational analysis, there was a compromise in terms of the phenomena studied, complexity of the objective (the more objective become complex, the more a structured mesh was recommended), computational time, and the required accuracy. For the UAS-S45 evaluated here, a structured mesh was considered in the airfoil analysis to evaluate the flow transition, the pressure distribution and the turbulence. Furthermore, an unstructured mesh has been used for the entire UAS-S45 computational analysis because of the fact that the aircraft flies at subsonic speeds.

2.1 Mesh Design of the S45 Wing Airfoil

The first step was the obtention of the aerodynamic coefficients of the airfoil, and the analysis of the flow around it, achieved by means of a 2D study of the UAS-S45 airfoil using ANSYS Fluent. The grid was generated with the Fluent meshing module; a structured mesh was selected rather than an unstructured mesh in order to align the velocity gradient with the mesh, thereby limiting dissipation errors. The use of a structured mesh was preferred, even though it is more difficult to generate it without a grid generator than an unstructured mesh, especially for complex geometry. The grid was generated using the "edge sizing" method shown in Fig. 3. ANSYS provides several options to control the size of the mesh cell, one of them being the "edge sizing". This method is used to specify the size or the number of divisions along an edge, and also the growth rate of the cells away from the edge. The "edge sizing" allows to obtain a sufficiently fine mesh to accurately capture the rapid changes inside the boundary layer. To use the "edge sizing", the distance between the first node of the mesh and the airfoil was calculated (Fig. 4). This distance also called "distance to the wall" is important to adequately resolve velocity gradients in the viscous sublayer of the boundary layer. The calculations were based on the flat-plate boundary layer theory from White's *Fluid Mechanics* 5th Edition [19]. The flow conditions used for the grid generation were: Reynolds number R_e = 8.17×10e6, altitude *alt* =10,000ft, and the Mach number M = 0.18. The characteristic length for the Reynolds number calculation was the mean aerodynamic chord of the airfoil c = 1 m.

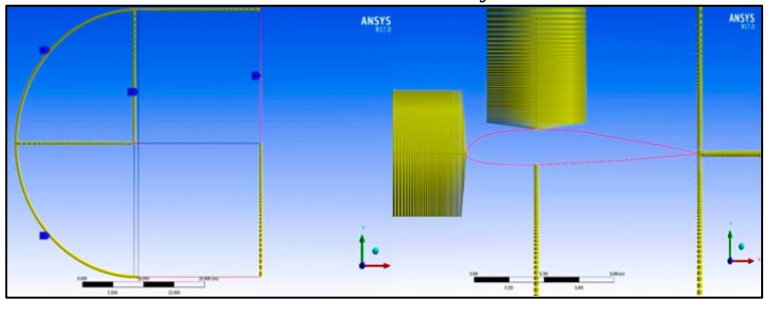

Fig. 3 Edge Sizing using Fluent

The grid spacing required to observe the turbulent phenomenon occurring around the airfoil for different flow conditions was found using the expressions from ref. [19]:

$$\mathrm{R_e} = \frac{\rho U_\infty L}{\nu} \tag{1}$$

$$C_F = 0.026\left(\mathrm{R_e}\right)^{-1/7} \tag{2}$$

$$\tau_\omega = \frac{C_F \rho U_\infty^{\,2}}{2} \tag{3}$$

$$U_\tau = \sqrt{\frac{\tau_\omega}{\rho}} \tag{4}$$

$$h = \frac{y^+ \nu}{U_\tau \rho} \tag{5}$$

By substituting Eqs. (1) – (4) in Eq. (5), Eq. (5) becomes:

$$\mathrm{h} = \frac{y^+ \mathrm{L}}{\sqrt{0.013 \mathrm{R_e}^{13/7}}} \tag{6}$$

In Eqs. (1) – (5), ρ is the air density, U_∞ is the freestream velocity, ν is the dynamic viscosity, C_F is the skin friction coefficient, τ_ω is the skin shear stress, U_τ is the friction velocity, L is the reference length, in our case, the mean aerodynamic chord, Re is the Reynolds number and y^+ is called distance to the wall, that refers to the distance between the first node of the mesh and the airfoil (Fig. 4); a small value of y^+ is recommended for boundary or viscous layer analysis but the number of cells of the mesh is increased.

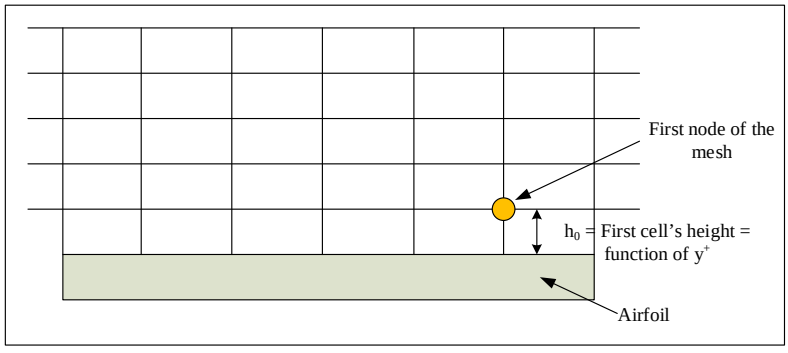

Fig. 4 First node and cell's distance definition

The first cell's height influences the value of y^+. To calculate the first cell's height, h_0, $y^+ = 1$ should be considered. However, because the Reynolds number is very high, a very small $h_0 = 8.12 \times 10\text{e-}6$ m was obtained (Eq. (19)), which led to a high number of cells and thus, an increase calculation time. Therefore, it is acceptable to consider $y^+ > 1$ to reduce the computation time. Furthermore, in order to fully analyze all the disturbances, and especially the phenomenon of separation, it is essential that y^+ lies in the viscous sub-layer which correspond, for a flat plate, to $0.1 > y^+ > 8$ according to the wall law (Fig. 5). According to the Fluent theory guide [20], with the chosen turbulence model, a value of $y^+=5$ was chosen, which corresponds to a first cell distance of $h_0=4{,}1\times 10\text{e-}5$ m. The mesh was constructed so

that the first cell was located at 0.04 mm from the airfoil, and the growth rate of the cells height never exceeded 1.2. Figure 6 shows the mesh around the airfoil.

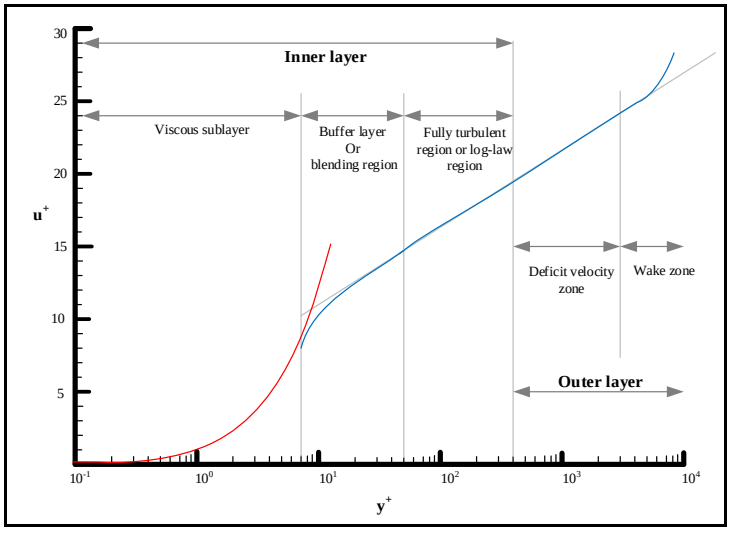

Fig. 5 Law of the wall [21]

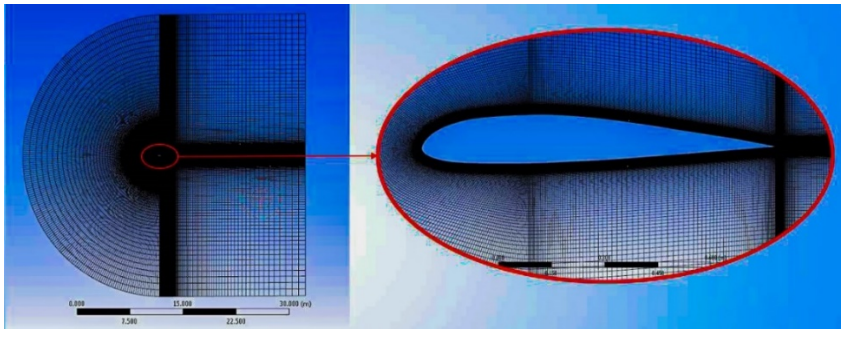

Fig. 6 Structured mesh grid around an S45 airfoil

The mesh was validated by checking the orthogonal quality and skewness of its cells that are two very good indicators of its quality. The orthogonality is the measure of how close the angles between adjacent element faces are close to an optimal angle [20] (90° for quadrilateral faces elements). A value close to 1 corresponds to a good orthogonality. The skewness is the measure of the difference between the shape of the cell and the shape of an equilateral cell of equivalent volume [20]. A value close to 0 corresponds to a good skewness. For the case of the UAS-S45 airfoil, the orthogonal quality was 0.978, while the skewness quality for the generated grid was 0.056 which indicate a good quality of mesh.

2.2 Mesh Design of the Entire S45-UAV

In the case of the entire UAS-S45, a grid convergence study was performed to evaluate the mesh density required for the aerodynamic coefficient estimations. Five mesh models were generated; each mesh was analysed at a Mach number of 0.14, an altitude of 0 ft and an angle of attack of 0 deg. Table 2 presents the statistics and the inflation parameters of each of the five generated meshes. The statistics parameters show the number of cells and node of the mesh and therefore give an overview of the complexity of the mesh and the calculation time needed to obtain a solution. The inflations parameters show the 1st layer thickness and the

maximum layers. The values of these parameters depend on the phenomena studied. For example, a small value of the 1st layer thickness is recommended for boundary layer analysis.

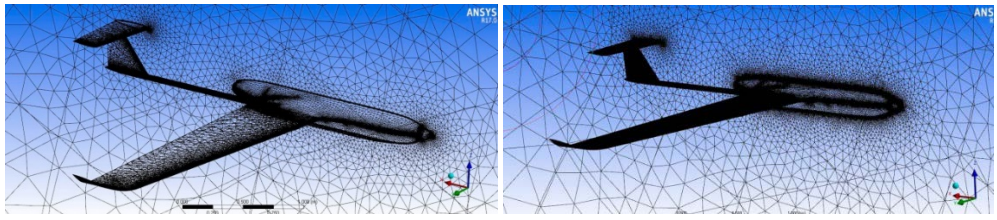

Fig. 7 UAS-S45 Mesh grid variation

Table 2. Parameters of the generated meshes

	Statistics parameters		Inflation parameters	
Mesh	Number of cells	Number of nodes	1st layer thickness (m)	Maximum layers
Mesh 1	1765718	413215	0.0006	8
Mesh 2	2989591	847864	0.002	5
Mesh 3	3349435	922813	0.002	5
Mesh 4	3942176	1173134	0.0006	8
Mesh 5	10158869	2722846	0.00006	8

Table 3. Results obtained for the grid convergence study

	Aerodynamic coefficients			Orthogonal quality of meshes	
Mesh	C_L	C_D	C_m	Min	Average
Mesh 1	0.167	0.019	-0.024	0.030514	0.84961
Mesh 2	0.161	0.020	-0.025	0.017939	0.85038
Mesh 3	0.166	0.020	-0.027	0.01305	0.85291
Mesh 4	0.162	0.019	-0.023	0.020536	0.8486
Mesh 5	0.167	0.019	-0.020	0.027141	0.83742

The aerodynamics lift and drag coefficients and the orthogonal qualities for each mesh model were calculated and further presented in Table 3. This table shows the differences in aerodynamic coefficients values obtained with mesh 5 versus the aerodynamic coefficients calculated with other meshes. Mesh 5 was selected as a reference mesh because of the fact that it contains the highest number of cells. A maximum relative error of 3% in C_L and C_D was found. For the design of an aerodynamic model of the UAS-S45, the first cell of the mesh may not be located in the viscous sublayer of the boundary layer. In fact, according to Eq. (19) for h, and for flight cases: Mach number M= 0.14, altitude alt =10,000ft, and wall distance of y^+=1, in order to resolve the viscous sublayer, the first cell should be located at 9.5×10e-6m from the aircraft, which is a very small value. This arrangement will result in a decrease in mesh quality and in a divergence in the simulation for a fixed number of cells because the phenomena complexity is increased but the number of cells is the same.

To avoid reducing the mesh quality, an appropriate sizing is required in order to create very small cells close to the aircraft, therefore an increase in the number of cells must be considered as well as the increase of the total simulation time. Therefore, as a compromise between the mesh quality and the number of cells, **mesh 2** was selected. Mesh 2 corresponds to a wall distance of y^+=200. To reduce computing time, the number of cells has been reduced

without decreasing the quality of the mesh by transforming the tetrahedral mesh into polyhedral mesh (Fig. 8). In some cases, the transformations can increase the quality of some cells located out of the boundary layer, but the cells of poorer quality (in general those in the inflation) remain unchanged since the transformation does not affect inflation. Table 4 shows the mesh model parameters used for the aerodynamics calculations.

Table 4. UAS-S45 mesh 2 model parameters

Parameter	Number of cells		1st layer height	Number of layers in the inflation	Orthogonal quality average	Skewness average
	tetrahedral	polyhedral				
values	3,349,435	1,049,508	0.002m	10	0.85291	0.26897

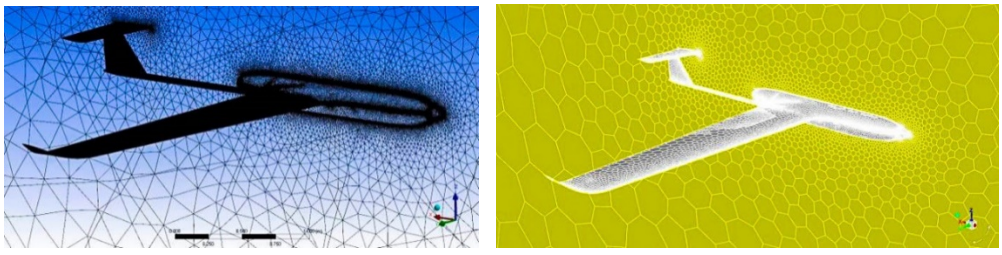

a) b)

Fig. 8 Tetrahedral mesh (a), polyhedral mesh (b)

3. CFD ANALYSIS. FLOW SOLVER

3.1 General Description of the Flow Solver

ANSYS Fluent software[20] was used to describe the pattern flow around the UAS-S45. ANSYS Fluent is capable of solving the Navier-Stokes equations for a wide range of incompressible and compressible, laminar and turbulent fluid flows. The software is useful to solve flow problems for various types of meshes, including unstructured meshes that can be generated about complex geometries relatively easy. Time integration is carried out using a three-stage explicit Runge-Kutta scheme. For steady-state flow simulations, convergence acceleration is achieved using local time stepping, residual smoothing, and a full-approximation storage multigrid. Setting the fluid flow for aerodynamic analysis using ANSYS Fluent includes defining the boundary conditions and the turbulence model.

3.2 Boundary Conditions

As a boundary condition for solving the UAS-S45 aerodynamics, the fluid is assumed to stick to the wall, and to move with the same velocity as it. Therefore, a no-slip condition was selected. A symmetry condition was also used at the symmetry plane of the UAS to reduce computation time.

3.3 Turbulence Model

By considering a turbulent flow, viscosity is assumed to not affect the larger-scale eddies, with the exception of the viscous sublayer in the boundary layer. The effects of the density fluctuations on the turbulence are assumed to be small. Thus, the direct effect of viscosity and compressibility on turbulence can be neglected [22]. The flow variables can be decomposed

into their time-average values and their fluctuating components. These assumptions lead to the Reynolds-Averaged Navier-Stokes (RANS) equations. The Boussinesq eddy-viscosity hypothesis was used to resolve the problem of "closure" by relating the Reynolds stress tensor and the turbulent heat flux to the average flow variables. The following equations are obtained:

$$\frac{\partial \rho}{\partial t}+\frac{\partial}{\partial x_j}(\rho U_j)=0 \tag{7}$$

$$\frac{\partial}{\partial t}(\rho U_i)+\frac{\partial}{\partial x_j}\left(\rho U_i U_j\right)=-\frac{\partial P}{\partial x_i}+\frac{\partial}{\partial x_j}\left[\mu_{eff}\left(\frac{\partial U_i}{\partial x_j}+\frac{\partial U_j}{\partial x_i}\right)-\frac{2}{3}\mu_{eff}\frac{\partial U_k}{\partial x_k}\delta_{ij}\right] \tag{8}$$

$$\begin{aligned}&\frac{\partial}{\partial t}\left(\rho H\right)-\frac{\partial P}{\partial t}+\frac{\partial}{\partial x_j}\left(\rho U_j H\right)=\frac{\partial}{\partial x_j}\left[\lambda\frac{\partial T}{\partial x_j}+\frac{\mu_t}{Pr_t}\frac{\partial h}{\partial x_j}\right]+\\&\frac{\partial}{\partial x_j}\left\{U_i\left[\mu_{eff}\left(\frac{\partial U_i}{\partial x_j}+\frac{\partial U_j}{\partial x_i}\right)-\frac{2}{3}\mu_{eff}\frac{\partial U_k}{\partial x_k}\delta_{ij}\right]+\mu\frac{\partial k}{\partial x_j}\right\}\end{aligned} \tag{9}$$

where ρ is the fluid density, U_i are the velocity components, P is the static pressure and μ_{eff} is the effective viscosity, which is the sum of the molecular viscosity μ and the turbulent viscosity μ_t, H is the total enthalpy, T is the fluid temperature, δ_{ij} is the Kronecker delta function, λ is the thermal conductivity, Pr_t is the turbulent Prandtl number, h is the static enthalpy and k is the turbulent kinetic energy [2]. For the UAS-S45 aerodynamic analysis, two turbulence models were added to the Reynolds-Averaged Navier-Stokes equations: The Spalart-Allmaras model for the entire UAS and the k-ω model for the UAS airfoil.

The single-equation Spalart-Allmaras model was used to estimate the turbulence kinetic energy, k. This model was designed and optimised for flows past wings and airfoils, and can be implemented for any type of grid [22]. The Spalart-Allmaras model determines the transported variable, $\tilde{\nu}$ which is identical to the turbulent kinematic viscosity except in the near-wall region. Equation (5) is thus added to the RANS equations [23].

$$\frac{\partial}{\partial t}\left(\rho\tilde{\nu}\right)+\frac{\partial}{\partial x_i}\left(\rho\tilde{\nu}U_i\right)=G_\nu+\frac{1}{\sigma_\nu}\left[\frac{\partial}{\partial x_j}\left\{\left(\mu+\rho\tilde{\nu}\right)\frac{\partial\tilde{\nu}}{\partial x_j}\right\}+C_{b2}\rho\left(\frac{\partial\tilde{\nu}}{\partial x_j}\right)^2\right]-Y_\nu \tag{10}$$

$$G_\nu=C_{b1}\rho\tilde{S}\tilde{\nu} \tag{11}$$

$$Y_\nu=C_{\omega1}\rho f_\omega\left(\frac{\tilde{\nu}}{d}\right)^2 \tag{12}$$

$$\tilde{S}\equiv S+\frac{\tilde{\nu}}{\kappa^2 d^2}f_{v2} \tag{13}$$

where G_ν is the production of turbulent viscosity, Y_ν is the destruction of turbulent viscosity that occurs in the near-wall region due to wall blocking and viscous damping, ν is the molecular kinematic viscosity, S is the measure the deformation tensor, d is the distance from the wall, f_ω and f_{v2} are empirical function of the turbulence model, $\sigma_{\tilde{\nu}}$ = 0.66, C_{b1} = 0.1355, C_{b2} = 0.622, $C_{\omega1}$ = 3.23, and κ = 0.4187 are constants. Since the Spalart-Allmaras model does not calculate the turbulent kinetic energy k, the terms related to the turbulent kinetic energy in the RANS equations are neglected. Eqs (8) and (9) become:

$$\frac{\partial}{\partial t}(\rho U_i)+\frac{\partial}{\partial x_j}\left(\rho U_i U_j\right)=\frac{\partial P}{\partial x_i}+\frac{\partial}{\partial x_j}\left[\mu_{eff}\left(\frac{\partial U_i}{\partial x_j}+\frac{\partial U_j}{\partial x_i}\right)\right] \tag{14}$$

$$\frac{\partial}{\partial t}(\rho H)-\frac{\partial P}{\partial t}+\frac{\partial}{\partial x_j}\left(\rho U_j H\right)=\frac{\partial}{\partial x_j}\left[\lambda\frac{\partial T}{\partial x_j}+\frac{\mu_t}{Pr_t}\frac{\partial h}{\partial x_j}\right]+\frac{\partial}{\partial x_j}\left\{U_i\left[\mu_{eff}\left(\frac{\partial U_i}{\partial x_j}+\frac{\partial U_j}{\partial x_i}\right)\right]+\mu\frac{\partial k}{\partial x_j}\right\} \tag{15}$$

The second turbulence model is the *k-ω* model. The *k-ω* model achieves high accuracy for boundary layers with adverse pressure gradient, and can be easily integrated into viscous sub-layers without any additional damping function [7, 22]. While the *k-ω* model has some weaknesses in flows with free stream boundaries, it can still give a very good estimation for general subsonic flows.

The *k-ω* model estimates the turbulence kinetic energy *k* and the specific rate of dissipation *ω* by adding two more equations to the RANS equations [24]:

$$\frac{\partial}{\partial t}(\rho k)+\frac{\partial}{\partial x_j}\left(\rho U_j k\right)=\rho P_k-\beta^*\rho\omega k+\frac{\partial}{\partial x_j}\left[\left(\mu+\sigma_k\mu_t\right)\frac{\partial k}{\partial x_j}\right] \tag{16}$$

$$\frac{\partial}{\partial t}(\rho\omega)+\frac{\partial}{\partial x_j}\left(\rho U_j\right)=\frac{\gamma\omega}{k}P_k-\beta\rho\omega^2+\frac{\partial}{\partial x_j}\left[\left(\mu+\sigma_\omega\mu_t\right)\frac{\partial\omega}{\partial x_j}\right] \tag{17}$$

where, ω is the specific rate of dissipation, P_k is the turbulent kinetic energy due to mean velocity gradients, and $\gamma = 0.52$, $\sigma_k = 0.6$, $\sigma_\omega = 0.5$ and $\beta = 0.06 - 1$, are the model's constants.

4. RESULTS AND DISCUSSIONS

In this chapter, the relative error is defined as being calculated between a reference value x_a and an approximated value x_b with the equation $\left|\frac{x_b - x_a}{x_a}\right| * 100\%$.

4.1 Airfoil Coefficients C_L and C_D Comparison

The methodology for estimating the airfoil aerodynamic coefficients using ANSYS Fluent was elaborated in Sections 2 and 3. The analysis of the S45 airfoil was performed for Mach number 0.18, Reynolds number 1.72×10^6, and a range of angles of attack from -20° to 20°. Lift and drag coefficients were obtained as well as their corresponding polar curves (C_L vs C_D) (Fig. 9).

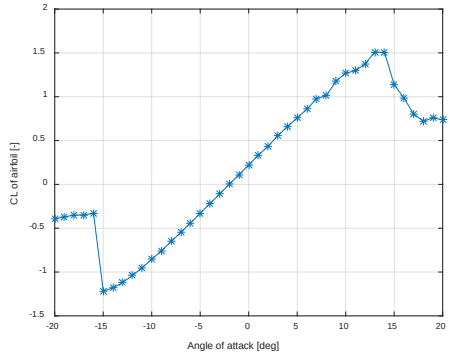

a)

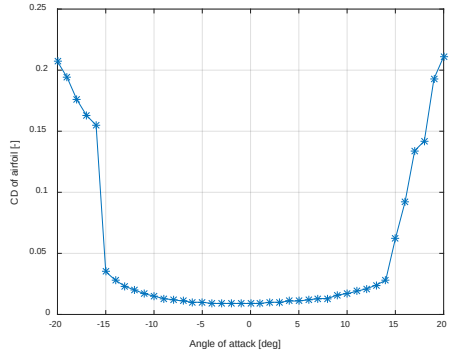

b)

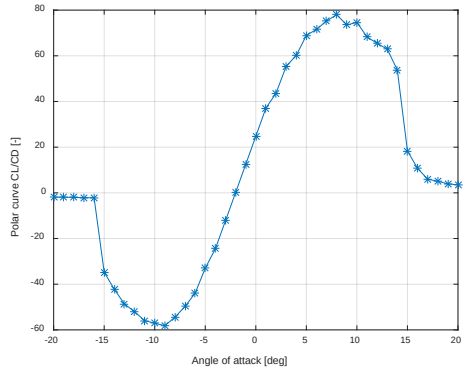

c)

Fig. 9 UAS-S45 airfoil lift coefficient, drag coefficient and polar curve variation with angle of attack for Mach number M=0.18

The evolution of the pressure distribution with angle of attack was also obtained. From Figure 10, it can be observed that for an angle of attack equal to 0°, there is a negative pressure on the upper wing surface which is causing the lift force creation. When the angle of attack becomes positive, the pressure on the upper surface decreases, and the pressure on the lower surface increases. Furthermore, for negative angles of attack, the pressure on the lower surface is less than the pressure on the upper surface. This analysis could be validated from airfoil aerodynamics theory point of view.

α=-10°

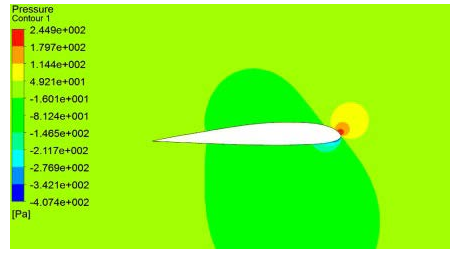

α=-4°

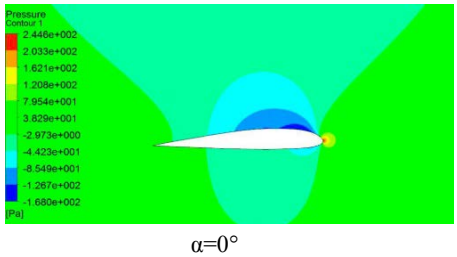

α=0°

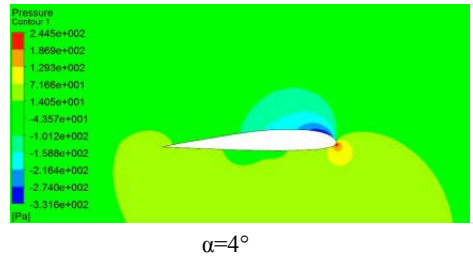

α=4°

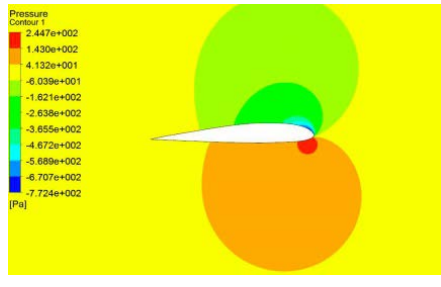

α=10°

Fig. 10 UAS-S45 airfoil pressure distribution with angle of attack

The results obtained with ANSYS Fluent were compared with those obtained using Xfoil software [25, 26]. XFoil is a program commonly used in research to estimate the aerodynamic coefficients of an airfoil for any given Reynolds and Mach numbers. The range of angles of attack was limited to -15° to 15° because of the stall, a phenomenon that is not accurately predicted using XFoil software. The results obtained with the CFD analysis were similar to those obtained with Xfoil for the linear region of the lift coefficient variation with angle of attack (Fig. 11). The agreement between results decreases around the angle of attack of 14° because of the beginning of the stall at this angle. Table 5 presents a comparison of five main aerodynamic parameters calculated with XFoil and ANSYS Fluent.

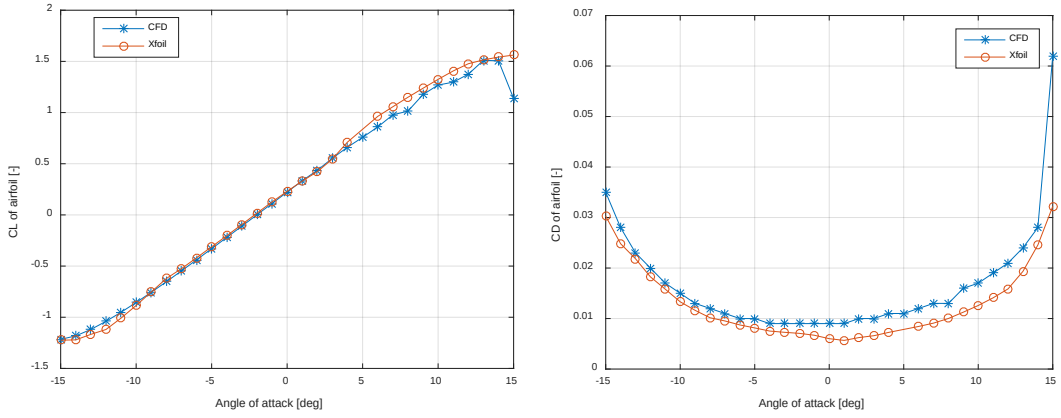

Fig. 11 UAS-S45 airfoil lift and drag coefficient variation with the angle of attack at Reynolds number = $1.72*10^6$ and Mach number = 0.18

Table 5. Airfoil parameter comparison

Parameters	**ANSYS Fluent**	**Xfoil**
Minimum drag coefficient, C_{Dmin}	0.009	0.005
Maximum lift coefficient, C_{Lmax}	1.51	1.56
Minimum lift coefficient, C_{Lmin}	-1.22	-1.16
Zero angle of attack lift coefficient, C_{L0}	0.22	0.23
Zero lift coefficient angle of attack, α_0	-2.011	-2.20

4.2 UAS-S45 Aerodynamic Coefficients' Comparison

The CFD analysis was performed for several different flight conditions, expressed in terms of Mach number, altitude and angle of attack, and for different aircraft configurations (Wing-Body, Tail, Wing-Body-Tail). The flight test cases are presented in Table 6.

Table 6. Flight test cases for determining the aerodynamic coefficients

Altitude [ft]	**Mach number [-]**	**Angle of attack [deg]**
0 – 20,000	0.10 – 0.2	-17 - 17

Figure 12 shows a comparison of the three aerodynamic coefficients C_L, C_D, C_m as function of three Mach numbers and for a range of angles of attack between -10° and 12° for a constant altitude of 10,000 ft. It can be observed that there is no important variation of the aerodynamic coefficients with the Mach number. This variation occurs because of the fact that the Mach number is less than 0.2 (subsonic), and thus the compressibility effects do not apply (Fig. 13).

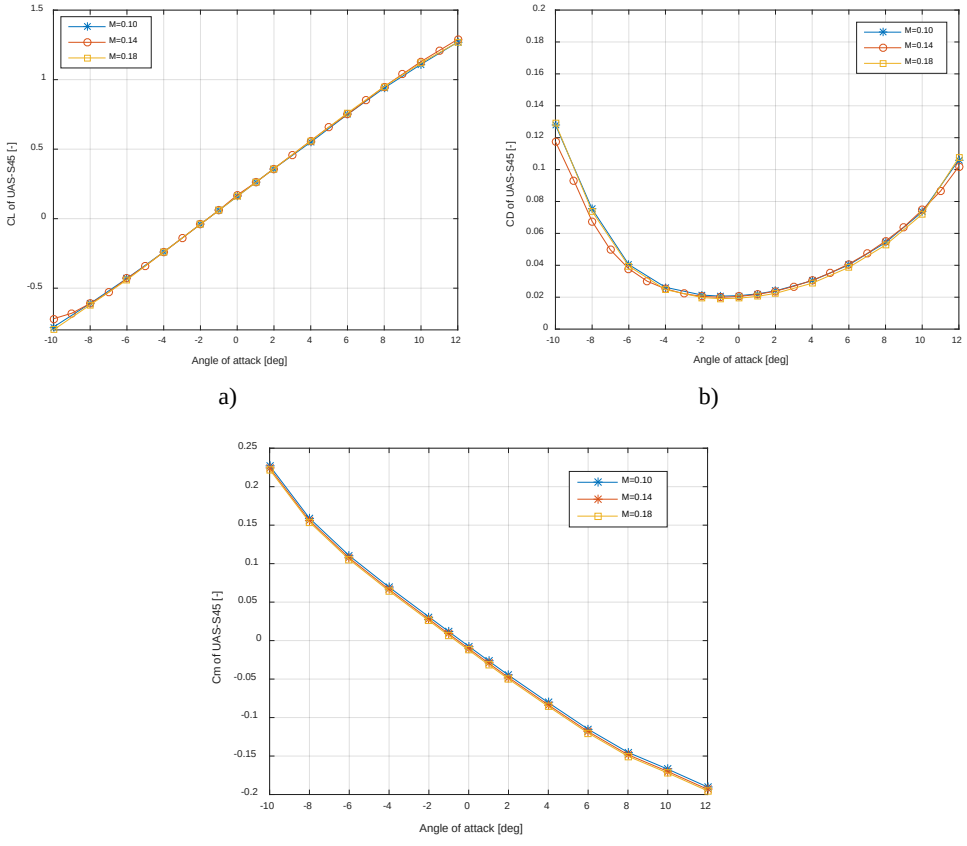

Fig. 12 Lift (a), drag (b) and pitch moment (c) coefficient variation with the angle of attack for the UAS-S45 at three Mach numbers below 0.2 for Altitude =10,000 ft

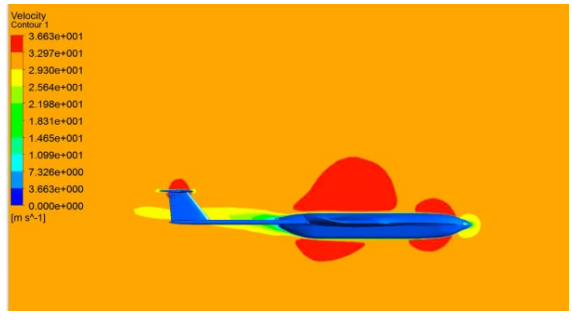

Fig. 13 Velocity contour around the UAS-S45

The same observation can be made for the drag coefficient variation with three altitudes and for a range of angles of attack between -10° to 12° for a constant Mach number of 0.14 (Fig. 14). The minimum drag, also known as the zero lift drag, does not change significantly with the altitude. Figure 15 displays a comparison between the entire UAS-S45 and the UAS-S45 in Wing-Body configuration. As expected, the Wing-Body configuration makes a major contribution to the aerodynamics of the entire UAS (as the variations of their results are very close). The pitch moment coefficient variation with the angle of attack confirmed the necessity of the horizontal tail. The Wing-Body pitch moment coefficient shows that the UAS-S45 in

the Wing-Body configuration is nearly stable, and that the horizontal tail (Fig. 15) acts as a lever, leading to a decreasing (more stable) pitching moment coefficient variation of the entire UAS-S45 with the angle of attack.

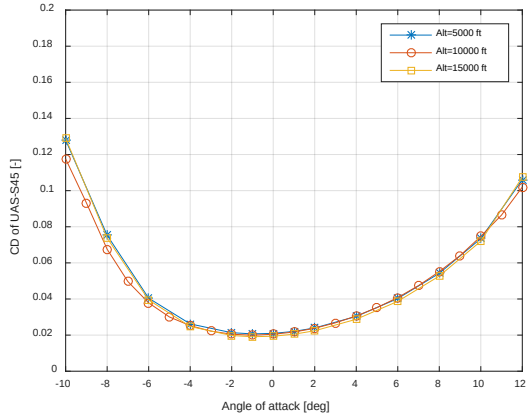

Fig. 14 Drag coefficient variation with the angle of attack for the UAS-S45 at several altitudes for Mach number = 0.14

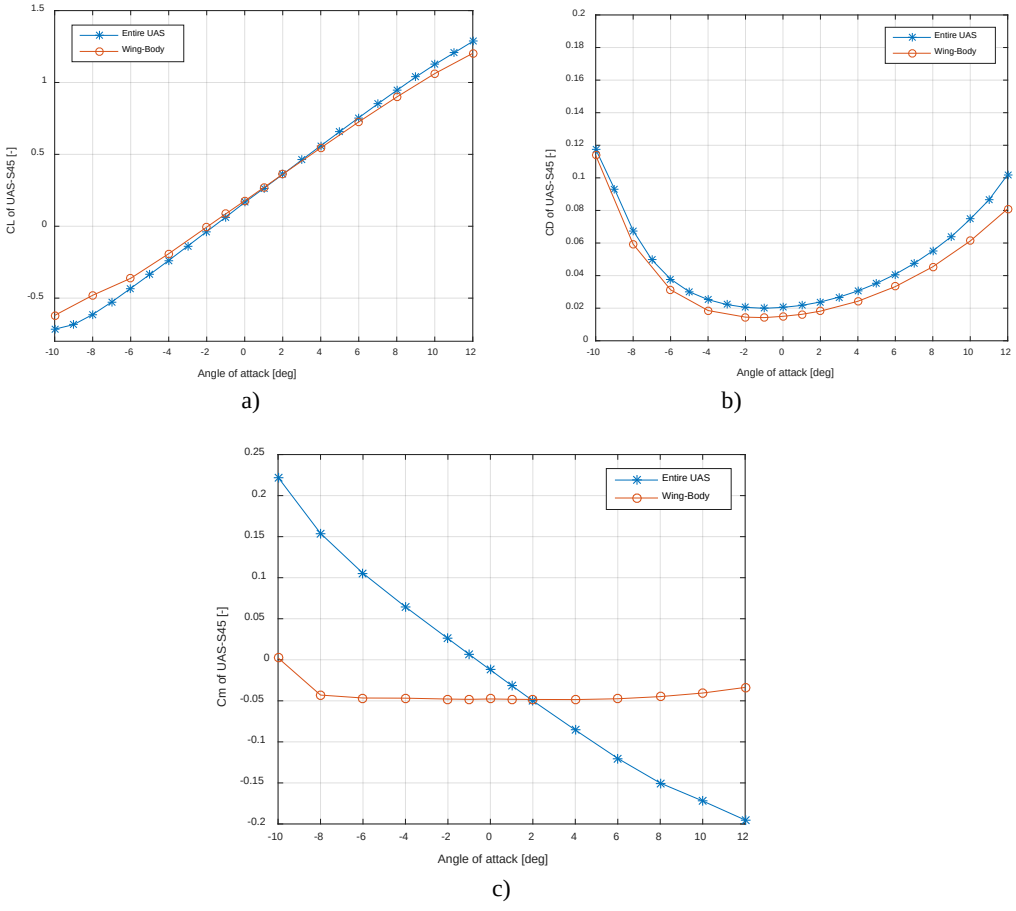

Fig. 15 Comparison of the lift (a), drag (b) and pitch moment (c) coefficients' variation with the angle of attack for the entire UAS-S45 and the "Wing-Body" configuration

The CFD results were thus compared with the nonlinear VLM results for the flight condition of Mach number = 0.14 and altitude =10,000ft. Fig. 16 shows the very good agreement of the results obtained. The zero-lift drag estimated using the nonlinear VLM was lower than the one estimated using the CFD analysis. This relative error was due the number of strips considered in the strip analysis, as the strip analysis was used to calculate the viscous pressure distribution on the wing surface. The increase of the number of strips also increased the computation time. A compromise must be done in fact between the computation time and the needed accuracy.

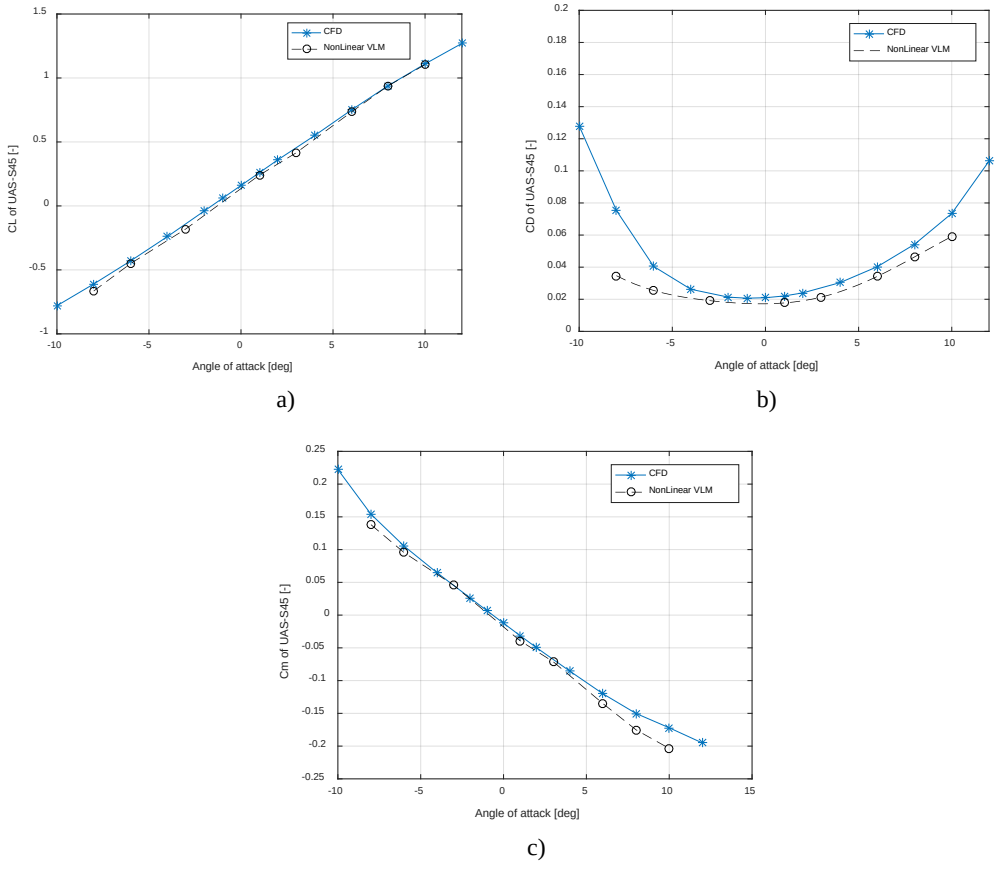

Fig. 16 Comparison of the lift (a), drag (b) and pitch moment (c) coefficients' variation with the angle of attack for the entire UAS-S45 obtained using the CFD analysis and the nonlinear VLM techniques

5. CONCLUSIONS

This paper presents a comparison between aerodynamics coefficient obtained using the new nonlinear Vortex Lattice Method formulation and a Computational Fluid Dynamics analysis. The computational fluid dynamics analysis was applied to the UAS-S45 geometry and airfoil. A structured mesh grid was generated for the UAS-S45 airfoil in order to align the velocity gradient with the mesh and limit dissipation errors. The first layer's thickness, the number of layers and the grid spacing were calculated using the law of the wall in order to study the viscous sublayer. An unstructured grid mesh grid was generated for the entire UAS-S45. A grid convergence study was made and an UAS-S45 mesh model was selected by taking into account a compromise between the accuracy of the results needed as well as the quality of the

mesh and the number of cells of the mesh. The Reynolds average Navier-Stokes equations were used to solve the flow equations around the aircraft with the Spalart-Allmaras model and the *k-ω* model as turbulence models.

This comparison reveals that a very close agreement between the methodologies. Thus, the aerodynamics model obtained using the nonlinear VLM and CFD can be used for efficient flight dynamics and control law modelling and simulation technologies. The next step will be the use of this code in the level D flight simulator design of the UAS-S45.

ACKNOWLEDGEMENTS

Special thanks are due to the Natural Sciences and Engineering Research Council of Canada (NSERC) for the Canada Research Chair Tier 1 in Aircraft Modelling and Simulation Technologies funding. We would also like to thank Mrs. Odette Lacasse and Mr. Oscar Carranza for their support at the ETS, as well as to Hydra Technologies' team members Mr. Carlos Ruiz, Mr. Eduardo Yakin and Mr. Alvaro Gutierrez Prado in Mexico for their collaboration.

REFERENCES

[1] T. E. Nelson, D. W. Zingg, Fifty Years of Aerodynamics: Successes, Challenges, and Opportunities, *Canadian Aeronautics and Space Journal*, **50**, 61–84, doi:10.5589/q04-003, 2004.

[2] O. Şugar Gabor, A. Koreanschi, R. M. Botez, M. Mamou, Y. Mebarki, Numerical Simulation and Wind Tunnel Tests Investigation and Validation of a Morphing Wing-Tip Demonstrator Aerodynamic Performance, *Aerospace Science and Technology*, **53**, 136–153, doi:10.1016/j.ast.2016.03.014, 2016.

[3] A. Koreanschi, O. Sugar-Gabor, R. M. Botez, Drag Optimisation of a Wing Equipped With a Morphing Upper Surface, *The Aeronautical Journal*, **120**, 473–493, doi:10.1017/aer.2016.6, 2016.

[4] R. M. Botez, M. J. T. Kammegne, L. T. Grigorie, Design, Numerical Simulation and Experimental Testing of a Controlled Electrical Actuation System in a Real Aircraft Morphing Wing Model, *The Aeronautical Journal*, **119**, 1047–1072, doi:10.1017/S0001924000011131, 2015.

[5] R. Pecora, I. Dimino, *SMA for Aeronautics*, In: Shape Memory Alloy Engineering, pp. 275–304, Butterworth-Heinemann, 2015.

[6] A. Salvatore, A. Brindisi, B. Tiseo, A. Concilio, R. Pecora, Optimization and Integration of Shape Memory Alloy (SMA)-Based Elastic Actuators Within a Morphing Flap Architecture, *Journal of Intelligent Material Systems and Structures*, **23**, 381–396, doi:10.1177/1045389X11428672, 2012.

[7] O. J. Boelens, CFD Analysis of the Flow Around the X-31 Aircraft at High Angle of Attack, *Aerospace Science and Technology*, **20**, 38–51, doi:10.1016/j.ast.2012.03.003, 2012.

[8] N. Anton, R. M. Botez, D. Popescu, Stability Derivatives for a Delta-Wing X-31 Aircraft Validated using Wind Tunnel Test Data, *Proceedings of the Institution of Mechanical Engineers, Part G: Journal of Aerospace Engineering*, **225**, 403–416, doi:10.1243/09544100JAERO799, 2011.

[9] O. Boelens, S. Goertz, S. Morton, W. Fritz, J. Lamar, F16-XL Geometry and Computational Grids Used in Cranked-Arrow Wing Aerodynamics Project International, *Journal of Aircraft*, **46**, 369–376, doi:10.2514/1.34852, 2007.

[10] J. W. Boerstoel, A. Kassies, J. C. Kok, S. P. Spekreijse, *ENFLOW a Full-Functionality System of CFD Codes for Industrial Euler/Navier-Stokes Flow Computations*, 1996.

[11] J. C. Kok, Resolving the Dependence on Freestream Values for the k- Turbulence Model, *AIAA Journal*, **38**, 1292–1295, doi:10.2514/2.1101, 2000.

[12] P. Panagiotou, P. Kaparos, K. Yakinthos, Winglet Design and Optimization for a MALE UAV using CFD, *Aerospace Science and Technology*, **39**, 190–205, doi:10.1016/j.ast.2014.09.006, 2014.

[13] M. Kuitche, R. M. Botez, *Methodology of Estimation of Aerodynamic Coefficients of the UAS-E4 Ehécatl using Datcom and VLM Procedure*, In: AIAA Modeling and Simulation Technologies Conference, p. 3152. American Institute of Aeronautics and Astronautics, Denver, Colorado (2017)

[14] O. Sugar Gabor, *Validation of Morphine Wing Methodologies on an Unmanned Aerial System and a Wind Tunnel Technology Demonstrator*, http://espace.etsmtl.ca/1614/, 2015.

[15] M. Rakowitz, B. Eisfeld, D. Schwamborn, M. Sutcliffe, Structured and Unstructured Computations on the DLR-F4 Wing-Body Configuration, *Journal of Aircraft*, **40**, 256–264, doi:10.2514/2.3117, 2003.

[16] T. Gerhold, M. Galle, O. Friedrich, J. Evans, T. Gerhold, M. Galle, O. Friedrich, J. Evans, *Calculation of Complex Three-Dimensional Configurations Employing the DLR-tau-code*, In: 35th Aerospace Sciences Meeting and Exhibit, p. 167, American Institute of Aeronautics and Astronautics, 1997.
[17] N. Kroll, Accurate and Efficient Flow Solvers for 3D Applications on Structured Meshes, In: *Computational Fluid Dynamics*, March 21-25, 1994.
[18] K. R. Laflin, *AIAA CFD Drag Prediction Workshop: an Overview*, Presented at the 25th ICAS Conference, 2006.
[19] F. M. White, *Fluid Mechanics*, McGraw-Hill Publishing Co., Boston (2003)
[20] * * * ANSYS: Fluent Theory Guide. ANSYS, INC, 275 Technology Drive Canonsburg, 2013.
[21] T. Von Kármán, *Mechanical similitude and turbulence*, National Advisory Committee For Aeronautics, Washington, D.C, 1931.
[22] C. D. Argyropoulos, N. C. Markatos, Recent Advances on the Numerical Modelling of Turbulent Flows, *Applied Mathematical Modelling*, **39**, 693–732, doi:10.1016/j.apm.2014.07.001, 2015.
[23] P. Spalart, S. Allmaras, *A One-Equation Turbulence Model for Aerodynamic Flows*, Presented at the 30th Aerospace Sciences Meeting and Exhibit, Reno, NV, USA, 1992.
[24] D. C. Wilcox, Formulation of the k-w Turbulence Model Revisited, *AIAA Journal*, **46**, 2823–2838, doi:10.2514/1.36541, 2008.
[25] M. Drela, *XFOIL: An Analysis and Design System for Low Reynolds Number Airfoils*, In: Low Reynolds Number Aerodynamics, pp. 1–12. Springer, Berlin, Heidelberg, 1989.
[26] J. Morgado, R. Vizinho, A. R. S. Miguel, P. Jose Carlos, XFOIL vs CFD Performance Predictions for High Lift Low Reynolds Number Airfoil, *Aerospace Science and Technology*, **52**, 207–214, doi:10.1016/j.ast.2016.02.031, 2016.